Plasma membrane domains enriched in cortical endoplasmic reticulum function as membrane protein trafficking hubs

Philip D. Fox[a,*], Christopher J. Haberkorn[a,*], Aubrey V. Weigel[b], Jenny L. Higgins[b], Elizabeth J. Akin[a], Matthew J. Kennedy[c], Diego Krapf[b,d], and Michael M. Tamkun[a,e]

[a]Department of Biomedical Sciences, [b]School of Biomedical Engineering, [d]Department of Electrical and Computer Engineering, and [e]Department of Biochemistry and Molecular Biology, Colorado State University, Fort Collins, CO 80523; [c]Department of Pharmacology, University of Colorado at Denver, Anschutz Medical Campus, Aurora, CO 80045

ABSTRACT **In mammalian cells, the cortical endoplasmic reticulum (cER) is a network of tubules and cisterns that lie in close apposition to the plasma membrane (PM). We provide evidence that PM domains enriched in underlying cER function as trafficking hubs for insertion and removal of PM proteins in HEK 293 cells. By simultaneously visualizing cER and various transmembrane protein cargoes with total internal reflectance fluorescence microscopy, we demonstrate that the majority of exocytotic delivery events for a recycled membrane protein or for a membrane protein being delivered to the PM for the first time occur at regions enriched in cER. Likewise, we observed recurring clathrin clusters and functional endocytosis of PM proteins preferentially at the cER-enriched regions. Thus the cER network serves to organize the molecular machinery for both insertion and removal of cell surface proteins, highlighting a novel role for these unique cellular microdomains in membrane trafficking.**

Monitoring Editor
Patrick J. Brennwald
University of North Carolina

Received: Dec 20, 2012
Revised: Jul 2, 2013
Accepted: Jul 2, 2013

INTRODUCTION

Trafficking of integral membrane proteins involves two separate but complementary processes: exocytosis mediated through SNARE (soluble *N*-ethylmaleimide–sensitive factor attachment protein receptor) complexes and endocytosis predominantly mediated by clathrin-coated pits (CCPs; Jahn and Sudhof, 1999; McMahon and Boucrot, 2011). In neuronal pre- and postsynaptic membranes, these processes are tightly localized to allow for rapid neurotransmitter release and activity-dependent synaptic plasticity (Sudhof, 2004; Sudhof and Rizo, 2011; Petrini *et al.*, 2009; Kennedy *et al.*, 2010). However, in other cell types, the localization of both processes has been debated. While studies in BSC-1 cells suggested that CCP initiation was randomly distributed over the cell surface during a 7-min observation period (Ehrlich *et al.*, 2004), CCPs have been shown to form, internalize, and reform at the same location in COS-1 cells (Gaidarov *et al.*, 1999). The existence of stable "hot spots" for clathrin-mediated endocytosis has now been described in many cell types (Toomre *et al.*, 2000; Keller *et al.*, 2001; Spiliotis and Nelson, 2003; Bellve *et al.*, 2006; McNiven, 2006; Rappoport *et al.*, 2006; Cao *et al.*, 2011; Nunez *et al.*, 2011). There are also examples of exocytosis reoccurring at stable sites in nonneuronal cells. In adrenal chromaffin cells, exocytic release occurs at specific reusable sites (Schroeder *et al.*, 1994; Robinson *et al.*, 1995, 1996; Wick *et al.*, 1997) and recent studies of Glut4 trafficking suggest specialized plasma membrane (PM) domains in adipose cells are used for Glut4 delivery to the cell surface (Stenkula *et al.*, 2010).

Recently we demonstrated that cell surface microdomains occupied by a voltage-gated K^+ channel, Kv2.1, function as hubs for Kv channel trafficking to and from the PM in both HEK cells and

This article was published online ahead of print in MBoC in Press (http://www.molbiolcell.org/cgi/doi/10.1091/mbc.E12-12-0895) on July 17, 2013.

*These authors contributed equally to this research.

Address correspondence to: Michael M. Tamkun (michael.tamkun@colostate.edu).

Abbreviations used: BAD, biotin acceptor domain; CCP, clathrin-coated pits; CDF, cumulative distribution function; cER, cortical endoplasmic reticulum; CLC, clathrin light chain; EDM, Euclidean distance map; EM, electron microscopy; ER, endoplasmic reticulum; GFP, green fluorescent protein; HA, hemagglutinin; MTT, multiple-target tracking; PM, plasma membrane; Qdot, quantum dot; RFP, red fluorescent protein; SEP, superecliptic pHluorin; TfR, transferrin receptor; TIRF, total internal reflection fluorescence; VSVG, vesicular stomatitis virus G-protein; YFP, yellow fluorescent protein.

cultured hippocampal neurons (Deutsch *et al.*, 2012). The delivery of Kv2.1 to the cell surface occurred at the edge of these micron-sized platforms, as did endocytosis. While it was perhaps not surprising that Kv2.1 would traffic at a location defined by the channel itself, we found that a completely unrelated K^+ channel (Kv1.4) was also delivered and retrieved at the Kv2.1 cluster perimeter. This finding suggested that the Kv2.1 clusters could function as generic endo- and exocytic platforms. Because the Kv2.1 clusters have been observed to localize with subsurface cisternae in hippocampal and motor neurons (Du *et al.*, 1998; Muennich and Fyffe, 2004) and to occasionally colocalize with ryanodine receptors (RyRs; Antonucci *et al.*, 2001), we explored the possibility that the Kv2.1 clusters preferred to localize over the cortical endoplasmic reticulum (cER), that is, endoplasmic reticulum (ER) that resides within 100 nm of the cell surface.

Here, using total internal reflection fluorescence (TIRF) microscopy in combination with multiple fluorescent markers for the ER, we demonstrate that this is indeed the case, with most of the Kv2.1 clusters residing above the cER. This result in turn raised the question of whether PM regions enriched in cER function as trafficking hubs for a variety of membrane proteins. We observed that both transferrin receptor (TfR) and Kv1.4 recycling occur immediately adjacent to regions of the PM enriched in underlying cER, suggesting stable endo- and exocytic machinery surround these domains. In addition, nascent vesicular stomatitis virus G-protein (VSVG) protein just released from the Golgi apparatus is delivered to the cell surface at these locations. Thus cER enrichment defines PM domains that function as trafficking hubs for membrane protein transport to and from the cell surface.

RESULTS

Cell surface Kv2.1 clusters are located at sites of cER enrichment

We first sought to determine whether Kv2.1-enriched trafficking hubs, which are specialized sites for Kv channel exo- and endocytosis (Deutsch *et al.*, 2012), are associated with specific intracellular structures, especially as previous studies suggested that Kv2.1 was often localized near subsurface cisternae (Du *et al.*, 1998). We therefore tested whether surface Kv2.1 clusters colocalized with peripheral ER projections. Figure 1A shows the relationship between surface Kv2.1 channel aggregates, detected via Alexa Fluor 594–conjugated antibody binding to an extracellular epitope inserted into Kv2.1 (red), and the ER, detected with ER-Tracker Green. This confocal section of a transfected HEK cell suggests a relationship between the surface clusters and the ER, with the clusters appearing at the end of finger-like projections of the cER network as highlighted by the yellow arrows in Figure 1B. A three-dimensional rendering of this cell region is presented in Supplemental Video S1. To confirm cER proximity at sites of Kv2.1, we used TIRF-based imaging to selectively visualize surface Kv2.1 and cER. HEK cells were transfected with green fluorescent protein (GFP)-Kv2.1 and DsRed2-ER to highlight the ER lumen, and the representative images shown in Figure 1, C–F, indicate that the majority of the Kv2.1 clusters colocalized with the ER marker within the TIR illumination field. Figure 1F is derived from only pixels with overlapping Kv2.1 and ER fluorescence and illustrates the surface distribution of the Kv2.1–cER interface. Kv2.1/ER colocalization was also observed when ER membrane proteins such as yellow fluorescent protein (YFP)-Stim1 were used to illuminate the ER (unpublished data). Supplemental Figure S1 shows that this Kv2.1 cluster localization over the ER is also observed in cultured hippocampal neurons. Because we had previously shown that

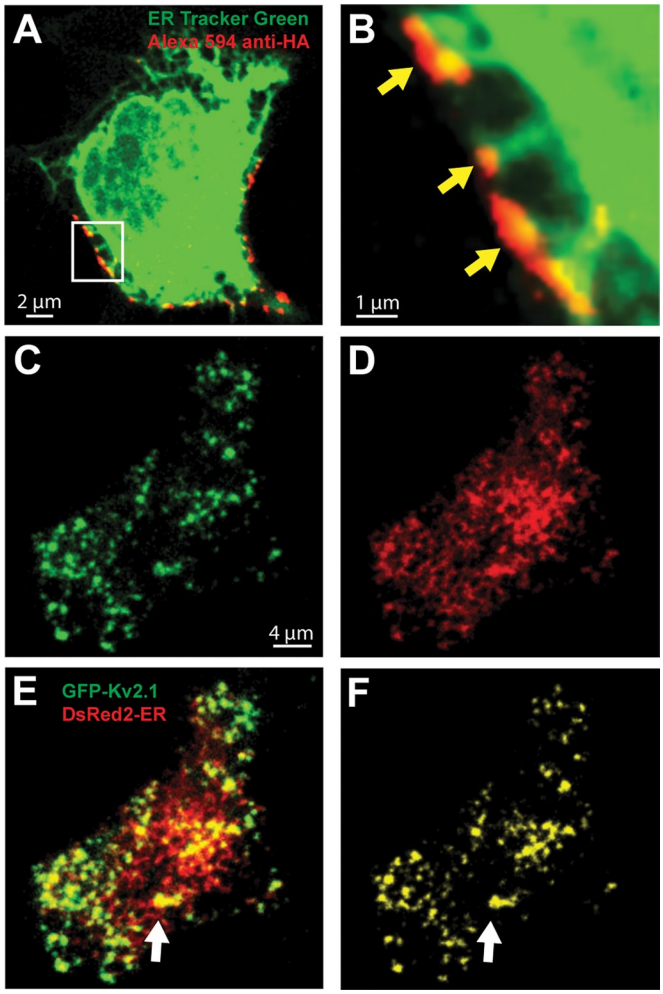

FIGURE 1: Kv2.1 cell surface clusters colocalize with the ER at the cell surface. (A) Confocal-based detection of Kv2.1-ER colocalization. Shown is a single confocal plane through the middle of a HEK cell transfected with Kv2.1HA. The ER was stained with ER-Tracker Green, and the red shows Alexa Fluor 594–conjugated anti-HA labeling of live cells to detect only surface Kv2.1 channels. (B) Enlargement of the boxed region in (A), illustrating the association of the Kv2.1 surface clusters (arrows) with cER finger-like projections. (C–E) TIRF-based detection of Kv2.1-cER colocalization. HEK cells were transfected with GFP-Kv2.1 and DsRed2-ER, and the corresponding fluorescence patterns are illustrated in (C) and (D), respectively. (F) Pixels containing both fluorescence signals. The thresholded Pearson's correlation coefficient for the cell in (C–F) was 0.61. For eight similar cells examined in TIRF, the correlation coefficient was 0.71 ± 0.07 (mean ± SD).

Kv2.1 surface clusters are sites for the exo- and endocytosis of Kv channels, we next asked whether cER enrichment defined PM domains that function as generic hubs for the trafficking of membrane proteins.

cER-enriched PM domains are the preferred site of TfR exocytosis

To observe exocytosis of a prototypical recycling membrane protein, we expressed the TfR fused to the pH-sensitive GFP variant superecliptic pHluorin (TfR-SEP) in HEK cells (Miesenbock *et al.*, 1998; Kennedy *et al.*, 2010). The SEP protein is attached to the extracellular domain of the TfR, so its fluorescence is quenched by the low pH of the endosome lumen. Trafficking vesicle fusion with

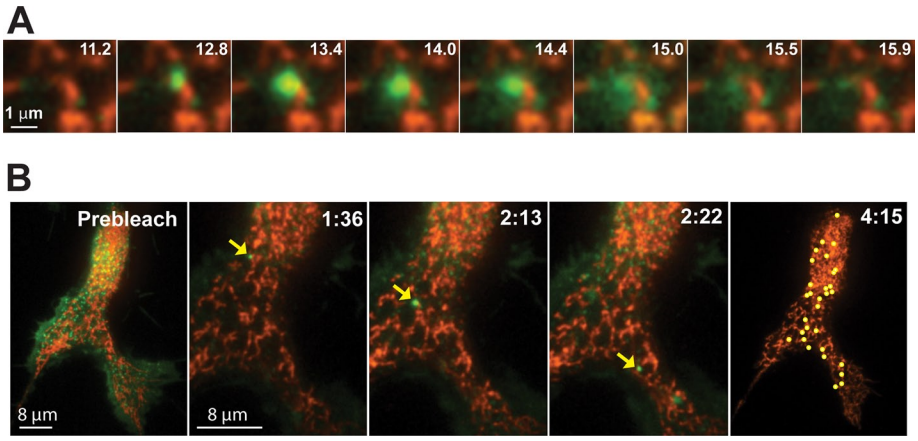

FIGURE 2: TfR exocytosis occurs at cER-enriched domains. (A) Time course of a single TfR-SEP exocytic event. Shown are TIRF images acquired over the indicated time series. (B) Localization of TfR-SEP exocytotic sites. Left panel, a TIRF image with the TfR-SEP localized to both the cER-associated puncta and the general PM. To enhance the signal-to-noise ratio of delivered TfR-SEP, we first bleached the basal membrane with high-power TIR illumination to reduce both the puncta intensity and, most importantly, the general membrane fluorescence derived from freely diffusing TfR-SEP molecules. The next three panels show single, bright puncta (yellow arrows) representing trafficking vesicles arriving post-bleach. Right panel, summary of the location of the delivery events observed up until the general membrane fluorescence became too bright to detect additional delivery. Sites of exocytosis are marked by the yellow circles.

the PM generates a burst of SEP fluorescence as the acidic pH is neutralized by the extracellular solution. This event is followed by lateral TfR diffusion in the PM and dispersal from the site of exocytosis. An example of one such exocytic event is shown in Figure 2A. A bright punctum suddenly appears adjacent to the cER (marked by DsRed2-ER) and disperses as the TfR-SEP diffuses away from the exocytic site over the next 1–2 s. To enhance the signal-to-noise ratio of delivered TfR-SEP, we first bleached the basal membrane with high-power TIR illumination to reduce membrane fluorescence derived from cell surface TfR-SEP. Figure 2B, left panel, shows a TIRF image of TfR-SEP and DsRed2-ER prior to TIR-based photobleaching. The next three panels show individual bright puncta (yellow arrows) representing trafficking vesicles arriving post-bleach. Such vesicular delivery is illustrated in Video S2, which contains the first 4 min of imaging following the TIR-based photobleach of this cell. The right panel of Figure 2B summarizes the location of the delivery events over the 6-min imaging session. In this example, 93% of the exocytic events occurred within 0.3 μm (2 pixels) of the cER perimeter. Overall 82 ± 12% (mean ± SD, $n = 560$, from 21 cells) of the TfR-SEP exocytotic events were adjacent to the cER near the PM. Exocytic events occurred either adjacent to or away from the cER-enriched regions, but never directly over the cER. For this reason, we measured the area occupied by only the perimeter of the cER, including a 0.3-μm zone outside the perimeter. The cER perimeter (0.3 μm) in these cells accounted for only 28 ± 8% of the cell footprint. This indicates that the cER-localized delivery is not simply random; that is, the occurrence of TfR fusion is disproportionately high at PM domains that are in close apposition to the cER. This observation was true not only for regions underneath the nucleus, where the cER is generally located, but also for peripheral regions. In these regions, 84 ± 7% ($n = 5$) of TfR-SEP delivery occurred within the cER perimeter, which only accounted for 31 ± 9% of the cell area. Similar findings were obtained with cultured hippocampal neurons as discussed in the Supplemental Material and illustrated in Figure S2A. For an additional control for random association with the cER perimeter, we expressed biotinylated Kv1.3 K^+ channels in HEK cells with the DsRed2-ER marker and labeled single channels with quantum dots (Qdots). Kv1.3 shows an evenly distributed localization on the cell surface and rapidly diffuses throughout the TIRF footprint. As illustrated in Figure S3, Qdot-labeled Kv1.3 channels have a random distribution with no relationship to the cER. Importantly, using our counting method, 42 ± 14% of Qdot-labeled Kv1.3 channels were located within 0.3 μm of the cER which occupied 41± 5% of the cell footprint ($n = 779$ Qdots in 6 cells). Together these data suggest that cER-enriched domains coordinate exocytotic machinery involved in surface protein delivery. Indeed, syntaxin 4 (Syx4), which is involved in neuronal exocytosis (Kennedy *et al.*, 2010), favors areas near the cER as illustrated in Figure S4. In 13 cells coexpressing Syx4-hemagglutinin (Syx4-HA) and DsRed2-ER, 68 ± 11% of stable Syx4 clusters were located within 0.3 μm of the cER perimeter while the cER perimeter represented 35 ± 8% of the cell footprint.

TfR exocytosis adjacent to the cER is statistically significant

To generate quantitative statistics demonstrating that the TfR exocytic sites are truly associated with the location of the cER, we adopted the use of Euclidean distance maps (EDMs; Russ, 2007). To our knowledge, this is the first application of this image-processing approach to cell biology. EDMs are generated from a binary image such that the features of interest, in our case cER structures, have a value of 0 ("off") and all other pixels have a value of 1 ("on"). The binary images were generated from filtered, thresholded, and zoomed TIRF images similar to those illustrated in Figure 2B. The Euclidean distance-mapping operation starts at the 0 values and sets all unassigned neighboring pixels to 1. The process then repeats iteratively, setting all unassigned neighbors of the pixels with a value of 1–2, their unassigned neighbors of pixels with a value of 2–3, and so on, until all pixels in the image have been assigned a value. This simple operation results in a new image in which each pixel value is the distance of that pixel to the nearest image feature, that is, the distance to the cER. TfR puncta were detected and localized at the moment of appearance using the U-track algorithm (Jaqaman *et al.*, 2008). Each delivery event was manually checked to ensure that only true exocytosis (as illustrated in Figure 2A) was analyzed. In addition, the selection was done without prior knowledge of cER location to avoid introducing human bias. The distance between delivery localization and the cER was then computed from the EDM, and the distribution of delivery distances from the cER was built.

If delivery to the PM occurred at random locations, independent of the ER, the distribution of distances between delivery location and cER would be, within statistical error, indistinguishable from the distribution of the EDM. This is a consequence of the EDM being the distribution of distances to the cER as computed for the pixels in the whole membrane image. Figure 3A shows the cumulative distribution function (CDF) of the distance between delivery and the cER as compared with the CDF of the distances of random pixels as obtained when the EDM of the entire TIRF footprint was used. The separation of the experimental and control curves indicates a clear

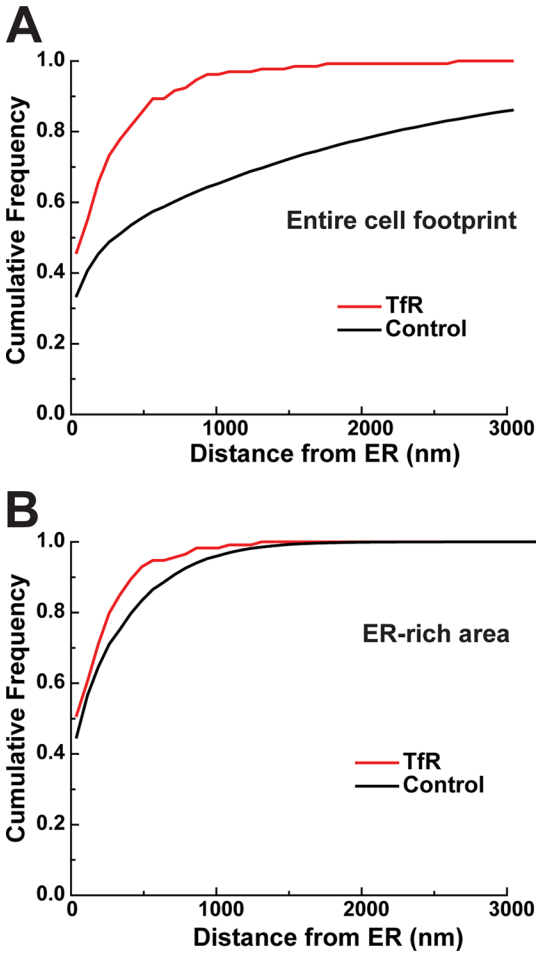

FIGURE 3: Euclidean distance mapping analysis of the sites of TfR exocytosis relative to the cER perimeter. Cumulative distribution functions (CDFs) comparing the distance of TfR exocytic sites from the cER (red) with the control case (black). Distances from the cER were determined by EDMs generated from images of the cER. (A) Summary data obtained using the entire TIRF footprint as determined from the low-level TfR fluorescence. The curve for the TfR plots the cumulative individual distances between the ER and exocytic locations. The control curve summarizes the distance to the ER for all the pixels present. The mean distance from the ER for TfR delivery was 0.25 ± 0.38 μm (mean ± SD, $n = 131$, from 5 cells), while the distance for the control pixels was 1.5 ± 2.6 μm, $p < 0.0001$. (B) Results derived from the region of the cell footprints highly enriched in cER. The mean distance from the cER for TfR delivery was 0.17 ± 0.24 μm ($n = 114$, from 5 cells), while the distance for the control pixels averaged 0.25 ± 0.33 μm ($n = 1.1 \times 10^7$ pixels), $p < 0.05$, assuming equal variance. The image crop forces the two curves together because now all pixels are relatively close to the ER.

preference for exocytosis at the cER, with 75% of the delivery events occurring within 0.25 μm of the cER perimeter, while the control curve generated from all the pixels in the footprint shows 75% of these pixels were within 1.75 μm of the ER. The mean distance from the ER for TfR delivery was 0.25 ± 0.38 μm (mean ± SD, $n = 131$, from 5 cells), while the distance for the control pixels was 1.5 ± 2.6 μm, $p < 0.0001$. The control curve was generated from 1.05×10^7 pixels. However, one could argue that delivery simply preferred the general region of the basal cell surface that was enriched in cER with no direct association with the cER itself. Therefore, we repeated this EDM analysis on regions of interest highly enriched in cER (Figure 3B). The results in cER-dense regions again indicate a preference for the cER. The separation between the curves is naturally reduced because the control pixels are now on average closer to the ER in the cropped images. The mean distance from the cER for TfR delivery was 0.17 ± 0.24 μm (mean ± SD, $n = 114$, from 5 cells), while the distance for the control pixels was 0.25 ± 0.33 μm, $p < 0.01$, assuming equal variance.

TfR is preferentially endocytosed at cER-enriched PM microdomains

When TfR-SEP was used to monitor exocytosis, we noticed that it formed small puncta that frequently associated with the cER (Figure 4, A and B). These puncta were likely on the cell surface, because the SEP fluorophore is pH sensitive. Overall 88.7 ± 5.5% ($n = 2609$, from 21 cells) of the TfR puncta were within 0.3 μm of the cER perimeter as detected with DsRed2-ER. The cER perimeter occupied 29 ± 8% of the cell footprint in these cells. Figure 4C illustrates the dynamics of the TfR-SEP puncta, where these structures repeatedly form in the same surface region before suddenly disappearing due to endocytosis and removal from the TIR illumination. All puncta in Figure 4C are TfR aggregates. The cyan and yellow puncta are derived from two video frames separated by 46 s. In most cases, adjacent blue and yellow puncta represent distinct TfR populations that disappeared and then reappeared in the same general region. When appearance was exactly in the same position, the color overlay is white. However, puncta lifetimes were variable, as was puncta mobility, and the white arrows denote puncta that did not disappear during the 46 s, sometimes moving and sometimes remaining stable. Video S3 illustrates the dynamics of the TfR-SEP

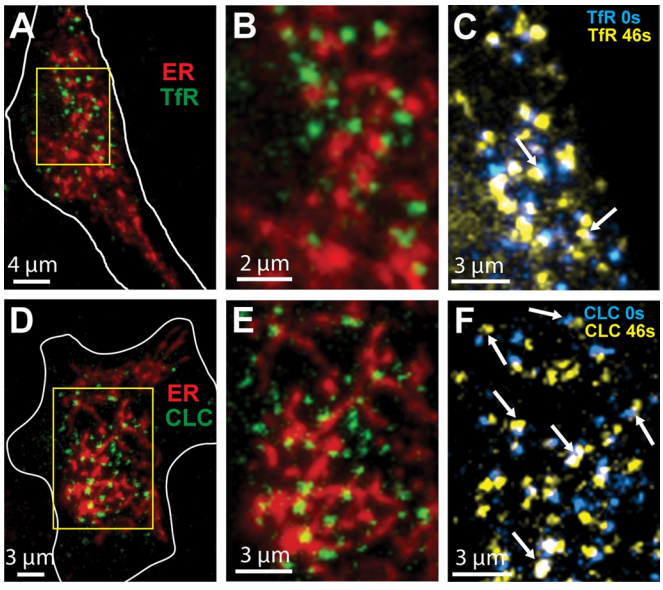

FIGURE 4: TfR and clathrin puncta localize adjacent to cER-enriched domains. (A) HEK cells were transfected with TfR-SEP and DsRed2-ER and then imaged using TIRF optics. The green TfR puncta are most often seen adjacent to, but not overlapping with, the cER marker. (B) Enlargement of the boxed region in (A). (C) TfR puncta present at two time points 46 s apart. Puncta present at 0 time are cyan, while those visible 46 s later are in yellow. The arrows point to puncta that either did not change or diffused a short distance (white). However, most puncta disappeared only to reform nearby over the 46 s. (D) HEK cells were transfected with GFP-CLC and DsRed2-ER prior to TIRF imaging. (E) Enlargement of the boxed region in (D). (F) CLC puncta detected 46 s apart, as described for (C).

puncta and shows the entire footprint of the cell from which the images in Figure 4, A–C, are derived.

Endocytosis of TfR is clathrin dependent, and TfR clustering in CCPs has been observed in numerous cell types (Hopkins, 1985; Jing *et al.*, 1990; Motley *et al.*, 2003; Bellve *et al.*, 2006). This led us to examine the relationship between CCPs and the cER. When GFP-clathrin light chain (GFP-CLC) was expressed in HEK cells with DsRed2-ER, diffraction-limited GFP-CLC puncta were frequently associated with the perimeter of the cER, reminiscent of the localization of TfR-SEP puncta (Figure 4, D and E). The GFP-CLC puncta had lifetimes ranging from 5 to 100 s, were mobile within a small radius, and often reformed within the same membrane region (as illustrated in Figure 4F and Video S4), consistent with previously published reports of CCP behavior (Gaidarov *et al.*, 1999; Ehrlich *et al.*, 2004; Loerke *et al.*, 2009; Saffarian *et al.*, 2009). Overall 88 ± 5% of the GFP-CLC puncta were within 0.3 µm of the cER perimeter (range 80–94%, $n = 1445$, from 10 cells). In these cells, the area encompassing the 0.3 µm surrounding the cER perimeter represented 44 ± 9% of the cell area, suggesting a robust preference for the cER-enriched domains. A similar relationship was observed in cultured hippocampal neurons (Figure S2B and Supplemental Material).

When TfR-SEP and red fluorescent protein (RFP)-CLC were cotransfected, the TfR-SEP puncta often colocalized with RFP-clathrin (Figure 5, A–D), confirming that many of the TfR-SEP puncta represent clathrin-based endocytic sites, as described in other cell types (Gaidarov *et al.*, 1999; Rappoport *et al.*, 2006). Even though the absolute intensities varied between puncta containing both TfR-SEP and RFP-CLC, the ratio of TfR-SEP to RFP-CLC fluorescence was relatively constant at 2.3 ± 0.4 (Figure 5E), consistent with previous reports demonstrating that CCPs grow as they accumulate cargo (Miller *et al.*, 1991; Loerke *et al.*, 2009; Mettlen *et al.*, 2010). Taken together, the data presented in Figures 4 and 5 strongly suggest TfR endocytosis occurs at stable, reusable sites adjacent to cER-enriched domains.

Delivery of post-Golgi carriers to the PM occurs at the perimeter of cER-enriched PM domains

In the case of the TfR, the measured exocytosis reflects the delivery of a recycling membrane protein, as opposed to a nascent protein trafficking directly from the Golgi to the cell surface. Thus the vesicles harboring these two different cargoes may be delivered to different microdomains on the cell surface. To examine the exocytic location of newly synthesized membrane proteins, we expressed a YFP-tagged, temperature-sensitive mutant of VSVG (YFP-VSVG-ts045), which remains unfolded in the ER at 40°C. After a switch to the permissive temperature (32°C), VSVG-ts045 can traffic through the Golgi network, where it buds off into vesicles that ultimately fuse with the PM (Presley *et al.*, 1997; Toomre *et al.*, 2000; Keller *et al.*, 2001). This creates a large number of exocytotic events against a relatively nonfluorescent background, enabling the identification of the site of exocytosis even without the aid of a pH-sensitive fluorescent protein. Exocytosis was examined in HEK cells expressing both DsRed2-ER and YFP-VSVG-ts045 following the shift to the permissive temperature. Figure 6A shows a HEK cell with blue dots marking the exocytic events that occurred within 0.3 µm of the cER perimeter and yellow dots marking exocytic delivery >0.3 µm from the cER perimeter. Figure 6B summarizes the location of exocytosis over time. Out of 52 exocytic events recorded in this cell, 46 of them occurred within 0.3 µm of the cER perimeter (only the first 33 events are illustrated in Figure 6, A and B). The majority of vesicles in this cell (36 of 52) appeared first at the cER perimeter; vesicle arrival was immediately followed by fusion at the cER or transient docking prior to fusion. However, in nine of 52 of these exocytic events, the vesicle appeared first at one cER perimeter before moving to a distant cER perimeter to fuse. This behavior is illustrated in Figure 6C, which shows a vesicle track (yellow line) following arrival at the cER perimeter (blue dot). The fusion or delivery site is indicated by a red "+." Vesicles with this behavior are also illustrated in Video S5. Together, these behaviors indicate that vesicles destined for fusion first appear in the TIRF field adjacent to cER-enriched domains. Generally, vesicles undergo fusion near the same cER domain where they first appeared. Vesicles that do not undergo fusion at the cER domain where they first appeared undergo fusion at a distant cER domain. Overall 84 ± 12% of exocytic events ($n = 213$, from seven cells) occurred within 0.3 µm of the cER, indicating a high degree of

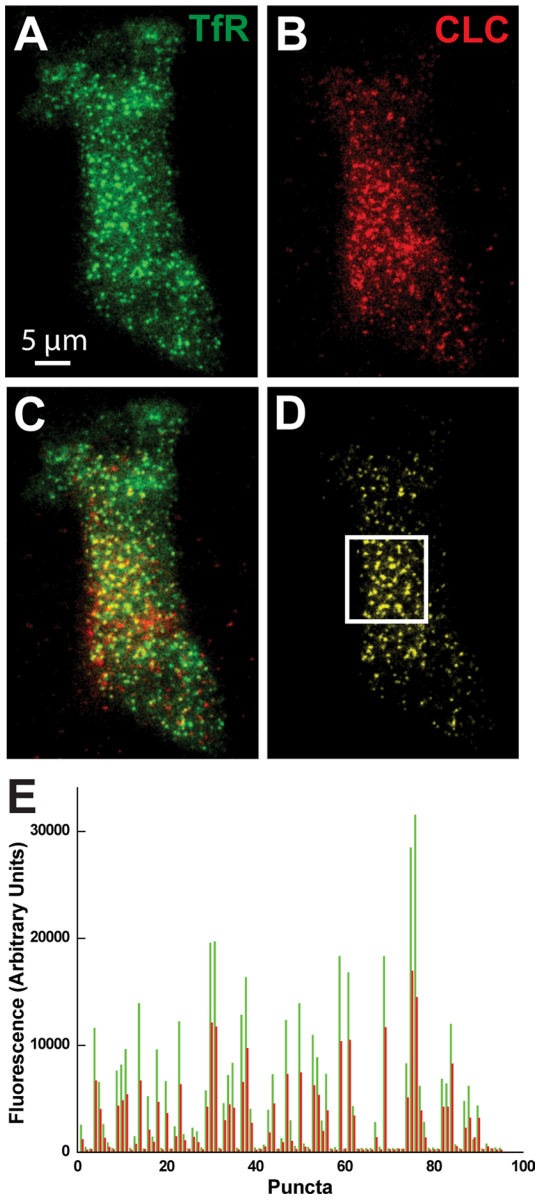

FIGURE 5: TfR-SEP and GFP-CLC puncta colocalize. (A and B) TIRF fluorescence pattern following transfection with TfR-SEP and RFP-CLC, respectively. (C) Traditional overlay of the TfR and CLC fluorescent signals. (D) Pixels containing only both fluorescence signals. (E) Ratio of TfR-SEP and RFP-CLC fluorescence of the puncta contained within the boxed region of (D).

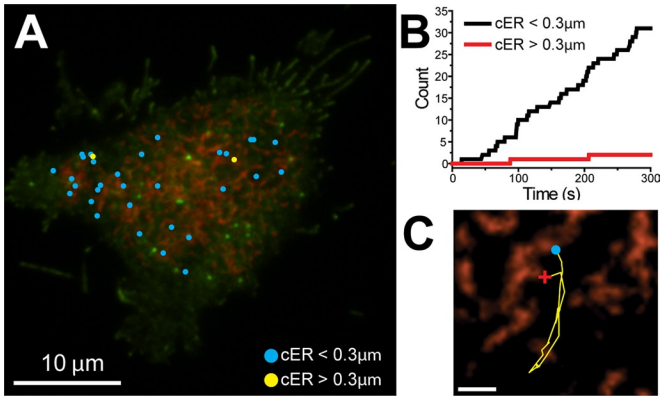

FIGURE 6: Exocytosis of VSVG-ts045 occurs predominantly at the cER perimeter. (A) HEK cell transfected with YFP-VSVG-ts045 and DsRed2-ER and imaged via TRIF microscopy at the permissive temperature (32°C). Blue dots mark exocytic events that occurred ≤0.3 µm from the cER perimeter, and yellow dots mark events that occurred >0.3 µm from the cER perimeter. Of 52 exocytic events recorded in this cell, 46 of them occurred within 0.3 µm of the cER perimeter; only the first 33 events are illustrated in (A) and (B). (B) Summary of the location of YFP-VSVG-ts045 vesicle fusion over time. Same cell as in (A). Overall 84 ± 12% of exocytic events (n = 213, from 7 cells) occurred within 0.3 µm of the cER perimeter. The cER perimeter (0.3 µm) in these cells was 28 ± 8% of the area of the TIRF footprint. (C) Magnification of DsRed2-ER fluorescence from (A) overlaid with a track of vesicular movement (yellow line). Appearance of the vesicle at the PM is marked with a blue dot, and exocytosis within 0.3 µm of the cER perimeter is marked with a red +.

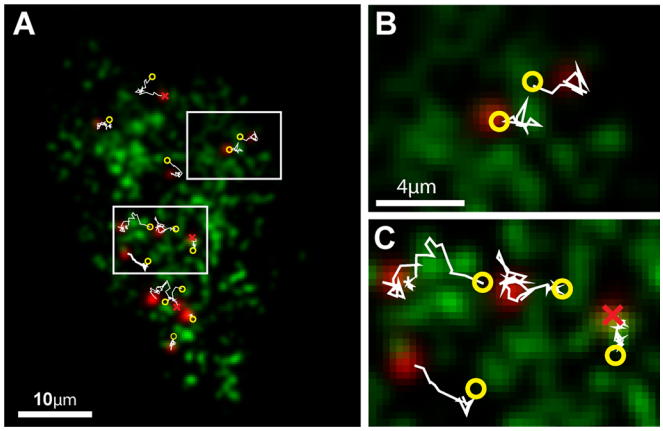

FIGURE 7: Exo- and endocytosis of Kv1.4. HEK cells expressing biotinylated Kv1.4 were labeled at low efficiency with 605 Qdots and then imaged via TIRF microscopy for observation of delivery and retrieval at the cell surface. (A) The location where the Qdot first appears is marked by the yellow circle, and its disappearance is marked with the red X. Note that the appearing Qdot in the top center of (A) most likely diffused into the TIR field from the side of the cell, as it was first detected at the edge of the cell. Trajectories from 292 frames are shown, and the length of the track is representative of the amount of time each Qdot was present during the movie. (B and C) Enlargements of the top and bottom boxed regions in (A), respectively. Kv1.4 exocytosis preferred PM sites within 0.15 µm of the cER perimeter with 78 ± 3% (n = 176 events, four cells) of Qdots spontaneously appearing in these regions. Kv1.4 endocytosis also preferred these regions with 77 ± 3% (n = 176 events, four cells) of Qdots spontaneously disappearing adjacent to the cER. In these cells, the cER perimeter (0.15 µm) accounted for only 21 ± 4% of the cell footprint.

association between exocytosis and cER-enriched domains. The cER perimeter (0.3 µm) in these cells was 28 ± 8% of the area of the TIRF footprint, again indicating that the cER-localized delivery is not simply random.

Recycling Kv1.4 potassium channels are both delivered to and retrieved from the cell surface near cER-enriched PM regions

We previously demonstrated that the Kv1.4 channel was delivered to and retrieved from the PM at the perimeter of Kv2.1 clusters (Deutsch *et al.*, 2012). To determine whether cER-enriched PM domains would still be the preferred site for Kv1.4 delivery and retrieval in the absence of Kv2.1 expression, we used a single-molecule, Qdot-based assay to track both exo- and endocytosis of recycling Kv1.4 channels. HEK cells expressing surface biotinylated CFP-Kv1.4-loopBAD (extracellular biotin acceptor domain) and DsRed2-ER were briefly incubated with a low concentration of Qdots to label a small fraction of the surface Kv1.4 channels. The cells were then imaged via TIRF, and the appearance and disappearance of Qdots were analyzed with custom tracking algorithms (Sergé *et al.*, 2008). As previously described (Deutsch *et al.*, 2012), the spontaneous disappearance of a Qdot for >60 s represents endocytosis, as nonfluorescent Qdot states are unlikely to occur for this amount of time. Similarly, the sudden appearance of a Qdot in the TIR field >60 s after the beginning of imaging represents membrane delivery of a previously internalized surface channel. Figure 7 illustrates the Kv1.4 insertion and retrieval sites mapped over 2 min and 42 s. The location where each Qdot first appears is marked by a yellow circle, and its disappearance is marked with a red X. Trajectories from 292 frames are shown, and the length of the track is representative of the amount of time each Qdot was present during the movie. Almost 80% of the Kv1.4 exocytosis (78 ± 3%, n = 176 events, four cells) occurred at PM sites within 0.15 µm of the cER perimeter. Nearly the same percentage of delivery events occurred at the perimeter of Kv2.1 clusters (Deutsch *et al.*, 2012). Kv1.4 endocytosis also preferred these regions, with 77 ± 3% (n = 176 events, four cells) of Qdots spontaneously disappearing adjacent to the cER. In these cells the cER perimeter (0.15 µm) accounted for only 21 ± 4% of the cell footprint.

Thin-section electron microscopy analysis of cER in HEK cells

The cER as viewed with TIRF-based light microscopy exhibited both tubular and punctate structures. At an ultrastructural level, we expected to see a similar pattern of ER running underneath PM. Our data also suggested that we would find both vesicular and endosomal structures near the cER. We analyzed the cER in glutaraldehyde-fixed HEK cells using thin-section electron microscopy (EM). To observe EM thin sections that most closely relate to our TIRF images, we began sectioning at the basal surface of the cells. Figure 8A gives us a TIRF-like snapshot of the basal membrane of the cell. Here we see ER that is likely within 100 nm of the PM, as it occupies the same plane as the sectioned basal membrane (B). Within 200 nm of the ER perimeter, we see four vesicular structures (V) that seem to be docked at the PM. These structures appear less dense in the center, suggesting they may be continuous with the extracellular space and thus in the process of exo- or endocytosis. Figure 8B is a deeper section, in which the ER makes a very small point of contact (black arrow) with the PM. We observed here both endocytic structures (white arrows) and vesicular structures in the immediate vicinity of the ER. The EM micrograph in Figure 8C illustrates a typical region of cER. Here the ER runs parallel to the PM at

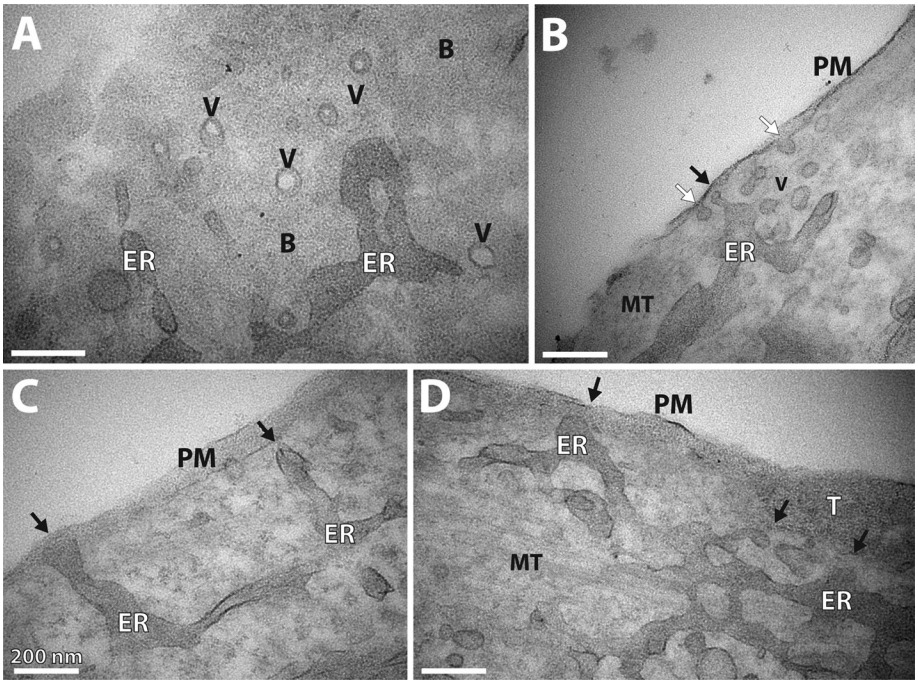

FIGURE 8: Thin-section EM of cER in HEK cells. (A) EM micrograph of an ultrathin section (<100 nm) through the basal membrane (B) of the cell. Within 200 nm of the ER (ER) on the right, there are four vesicular structures (V), which are likely docked at the PM. (B) EM micrograph illustrates ER making a small contact point (black arrow) with the PM (PM) in this section. Endocytic structures (white arrows) and possible vesicular structures are within 200 nm of the ER–PM contact point. (C) This EM micrograph illustrates a typical region of cER. Here the ER runs parallel to the PM but at a distance >100 nm from the PM. The ER turns to make perpendicular contacts with PM (black arrows). (D) This micrograph illustrates a similar situation as in (C), with the ER running parallel to and making contacts with the PM. Microtubules (MT) run underneath the cER at a distance far out of the TIRF field. All micrographs were acquired at 100,000× magnification. All scale bars are 200 nm. (B = basal membrane; V = vesicular structure; PM = cross-sectioned PM; MT = microtubules; T = transverse-sectioned PM; black arrows = ER–PM contacts; white arrows = endocytic structures).

a distance >100 nm away, likely not within the field of view that can be imaged by TIRF microscopy. The ER turns outward to make occasional perpendicular contacts (black arrows) with the PM. Figure 8D illustrates a similar situation, with the ER running parallel to the transversely sectioned PM (T) and occasionally making close contact with the PM. Here some of the tubular ER running parallel to the PM is close enough (<100 nm) to be observed in the TIR imaging plane. This is consistent with the often tubular appearance of the cER in TIRF. Microtubules run underneath the ER at a distance far beyond TIR imaging plane. Distinct ER–PM junctions like those found in subsurface cisterns in neurons (Rosenbluth, 1962) or induced by STIM1 in response to ER Ca^{2+} depletion (Orci *et al.*, 2009) were rarely observed in our HEK cells.

Our ultrastructural study of cER in HEK cells shows that some of the cER we observe in TIRF indeed forms close physical contact with the PM. To study these apparent connections in greater detail with TIRF microscopy, we expressed YFP-STIM1, which is a well-characterized marker for ER–PM contacts, along with DsRed2-ER. YFP-STIM1 is distributed throughout the ER under normal resting conditions but displays a remarkable translocation to sites of contact between the ER and PM under conditions of ER Ca^{2+} depletion (Liou *et al.*, 2005). We observed that YFP-STIM1 translocated to a subset of discrete cER-enriched domains, consistent with our ultrastructural analysis (Figure S5). To determine whether ER–PM contacts are involved in the localization of trafficking events near the cER perimeter, we repeated our TfR exocytosis study using ORAI1 as a marker for ER–PM contacts. ORAI1 is a PM Ca^{2+} channel physically gated by interactions with activated STIM1 in the ER. ORAI1 typically has a diffuse PM localization and only localizes to ER–PM contacts following physical interaction with STIM1 (Figure S6B). When we used ORAI1 puncta as a marker of ER–PM contacts, we observed 67 ± 5% (n = 5, 150 events) of TfR exocytic events occurred within 2 pixels of the ORAI1 puncta, while the puncta only accounted for only 15 ± 3% of the cell footprint (Figure S6C). These data indicate that a subset of the cER-localized TfR exocytosis occurs in the vicinity of "classic" ER–PM contacts.

DISCUSSION

The previously described function for cER largely involves regulation of Ca^{2+} homeostasis. In the PM, voltage-gated Ca^{2+}, Orai, and Trp channels are localized to these microdomains along with ER proteins involved in Ca^{2+} regulation, such as the ryanodine receptor, IP3 receptor, and STIM1 (Carrasco and Meyer, 2011). The data presented above indicate that an additional role for these membrane domains is to serve as localized trafficking hubs for endo/exocytosis. Not only are the relatively abundant TfRs trafficked at these locations but also sparse membrane proteins, such as the Kv1.4 K^+ channel. In addition, this localized trafficking extends beyond recycling membrane proteins, because nascent VSVG traveling to the surface for the first time is delivered here. While the work presented here is derived from HEK cells, the data are likely of general relevance to other cell types, especially neurons. HEK cells express a large number of neuronal genes and are actually of neuronal origin, despite the fact that they were derived from a kidney homogenate (Shaw *et al.*, 2002). Because HEK cells express almost no voltage-gated ion channels, they are best viewed as immature neurons. Furthermore, a recent publication describes a strikingly similar relationship between the cER and endocytic traffic in yeast, in which the cER extends across the majority of the PM (Stradalova *et al.*, 2012).

Advantages of localized trafficking hubs

Research over the past decade has increasingly demonstrated that numerous PM functions are highly organized, often due to the existence of specific submembrane scaffolding structures. The use of stable, reusable sites for endo/exocytosis outside the neuronal synapse is now becoming a commonly accepted idea (Schroeder *et al.*, 1994; Robinson *et al.*, 1995, 1996; Wick *et al.*, 1997; Bellve *et al.*, 2006; Stenkula *et al.*, 2010). Membrane protein trafficking hubs, as described here and in our previous work, have obvious advantages. Specialized domains are more energy efficient than constantly reassembling trafficking machinery, and trafficking vesicles can be delivered along relatively static microtubules. Such localization also provides for enhanced regulation, because signaling molecules can be stably localized at the trafficking sites.

Why cER-enriched PM domains as a trafficking hub?

Using this cellular organelle as a trafficking hub has two obvious advantages. First, many trafficking vesicles delivering cargo to the cell surface move via kinesin motors along microtubule tracks. The ER network is rich in microtubules, with microtubule dynamics responsible for defining cytoplasmic ER morphology (Terasaki *et al.*, 1986; Klopfenstein *et al.*, 1998; Waterman-Storer and Salmon, 1998). Thus the ER surface itself may serve as a template for microtubule orientation toward the cell surface. Second, because the cER plays a major role in Ca^{2+} homeostasis, trafficking here could place endo/exocytosis under direct control of Ca^{2+} within this microdomain. In support of this idea, ER-derived Ca^{2+} regulates exocytosis in astrocytes (Marchaland *et al.*, 2008). While this study specifically examined glutamate release from these cells, this effect of localized Ca^{2+} on exocytosis may have general relevance.

Relationship between the cytoskeleton, cER, and exocytosis

An obvious concern is that cER reaches the PM in regions where cortical actin is sparse and these just happen to be areas where exocytic/endocytic vesicles can get access to the PM (Orci *et al.*, 1972). We have addressed this possibility in two ways. First, as illustrated in Figure S7, we disrupted F-actin with latrunculin A (100 nM, 30 min) and observed the ER present at the cell surface decreasing to 77 ± 12% of control ($n = 12$). If the ER, and trafficking vesicles, reach the surface just where cortical actin is sparse, then actin depolymerization should have increased the amount of ER visible within the TIR field. Actin depolymerization caused a decrease in the percentage of TfR exocytotic events occurring at the ER perimeter, from 82 ± 12% (mean ± SD, $n = 560$, from 21 cells) under control conditions to 76 ± 9% (mean ± SD, $n = 97$, from four cells). However, it is difficult to conclude that F-actin is involved in coupling exocytosis to the ER perimeter, because this change could be due to nonspecific effects derived from cell shape changes following loss of the cytoskeleton. In our second attempt to relate cER and actin, we imaged photoactivatable GFP-actin and DsRed2-ER in TIRF and found that, while large actin bundles appear to direct the cER morphology, fluctuations in the fluorescence intensity of the finer cortical actin mesh, which cannot be resolved by light microscopy, show no apparent relation to ER positioning (Figure S8). Additional research is required to determine the role, if any, of actin in the localization of exocytosis near the cER.

On the other hand, microtubules play a role in both the organization of the ER and vesicular transport. This led us to investigate whether tubulin disruption with colchicine alters the cER or the location of TfR exocytosis. While the cytoplasmic ER is disrupted following microtubule depolymerization with colchicine (2.5 μM, 20 min, $n = 5$) as expected (unpublished data), the ER in the TIR field is unaffected, as illustrated in Figure S9, suggesting tubulin does not play a tethering role for the cER. After 40 min in colchicine, the percentage of TfR exocytosis occurring within 0.3 μm of the cER perimeter is reduced to 47 ± 18% ($n = 9$) compared with 82 ± 5% under control conditions, with the cER perimeter representing 24 ± 7% of the cell area. Whether this is meaningful or just an indication of poor cell health, as suggested by the morphology changes, is unclear. Unfortunately, we have found no interventions that selectively remove the cER, for this would be a convincing means of linking this structure to exocytosis.

Conclusion

We have discovered a new cellular microdomain that directs membrane protein trafficking to and from the cell surface. Exocytosis of both recycling and nascent membrane proteins preferentially occurs adjacent to sites of close apposition between the cER and the PM. Furthermore, endocytic components, such as CLC and TfR cargo, preferentially accumulate adjacent to cER-enriched PM domains. This spatial arrangement suggests that factors important for the localization and regulation of exo/endocytic machinery are enriched in the vicinity of the cER.

MATERIALS AND METHODS

Plasmid constructs, cell culture, and transfections

Fluorescent protein, HA epitope, and BAD-tagged Kv channel constructs have been described previously (O'Connell and Tamkun, 2005; O'Connell *et al.*, 2006, 2010; Tamkun *et al.*, 2007) and are based on the Living Colors vector system (Clontech, Mountain View, CA). The HA epitope or BAD sequence is contained within the extracellular domain between the first and second transmembrane domains of Kv2.1 and Kv1.4 (Tamkun *et al.*, 2007; Weigel *et al.*, 2011). When necessary, the BirA biotin ligase in the pSec vector was cotransfected with Kv1.4 to achieve biotinylation during channel biosynthesis, presumably within the ER lumen (Tamkun *et al.*, 2007). TfR modified with an extracellular SEP has been previously described (Kennedy *et al.*, 2010). The temperature-sensitive VSV G-ts045 fused to YFP has also been described previously (Presley *et al.*, 1997). CLC with GFP or RFP fused to the C-terminus was a gift from Santiago Di Pietro (Department of Biochemistry and Molecular Biology, Colorado State University). The luminal ER marker pDsRed2-ER was obtained from Clontech.

HEK 293 cells (passage 38–45; American Type Culture Collection, Manassas, VA) cells were transfected with 1–3 μg of Kv channel DNA, 1 μg of pSec Bir A, 100 ng of CLC fusions, 500 ng of TfR-SEP,200 ng of DsRed2-ER, or 1 μg of YFP-VSVG-ts045 using a Bio-Rad Genepulser Xcell (Bio-Rad Laboratories, Hercules, CA) with a 0.2-cm gap cuvette and a single 110-V 25-ms pulse. Transfected cells were plated on glass-bottom 35-mm dishes (Matek, Ashland, MA) that had been previously coated with Matrigel (BD Biosciences, San Jose, CA) and covered in DMEM plus 10% fetal bovine serum. HEK cells were imaged within 24 h of electroporation in HEK physiological imaging saline consisting of (in mM): 146 NaCl, 4.7 KCl, 2.5 $CaCl_2$, 0.6 $MgSO_4$, 1.6 $NaHCO_3$, 0.15 NaH_2PO_4, 0.1 ascorbic acid, 8 glucose, and 20 HEPES (pH 7.4; imaging saline).

Confocal and TIRF microscopy

HEK cells and neurons expressing fluorescent protein–tagged constructs were imaged with one of two microscope systems, depending on the experiment performed. Standard three-dimensional imaging, 0.3-μm Z steps, was performed with an Olympus FV1000 confocal microscope equipped with spectral detectors and the SIM scanner. GFP was excited using the 488-nm line of an argon laser, and emission was collected using the variable band-pass filter set at 500–530 nm. Alexa Fluor 594 fluorophores were detected using a 543-nm HeNe laser with the variable band-pass filter set at 600–630 nm. A 60×/1.4 NA oil-immersion objective was used for imaging, and the pinhole diameter was set for the appropriate Airy unit when using one laser. An intermediate pinhole diameter was used when two fluorophores were being detected simultaneously. For each image, the detector voltage was adjusted as necessary to utilize the full 12-bit range.

To image Qdot recycling and cER, we used a Nikon Eclipse Ti Perfect-Focus–equipped TIRF/wide-field fluorescence microscope equipped with AOTF-controlled 405-, 488-, 543-nm diode lasers, 100 mW each, and an Intensilight wide-field light source. A 100× Plan-Apo TIRF, 1.49 NA objective was used for image acquisition. Emission was collected through a Sutter Lambda 10-3 filter wheel

containing the appropriate band-pass filters. The stage and objective are temperature controlled via a Zeiss/Pecon stage-heating insert and objective heater at 37°C. This microscope is equipped with the Andor iXon EMCCD DU-897 camera, 512 × 512. For all imaging experiments, the cells were on the microscope stage for less than 1 h.

cER domain localization

The majority of experiments used DsRed2-ER expression to illuminate the cER in TIRF with a calculated penetration depth of 63 nm. The cER-enriched domains were delimited by an automated object-finding algorithm (Volocity, version 6.1.1; Waltham, MA), and the cER perimeter was calculated automatically. Neither exocytic events nor clathrin-related structures were observed to localize directly over the cER, so the area occupied by the cER-enriched domains was not included in the calculation of cER perimeter. For confocal imaging, cells were labeled for 10 min at 37°C with ER-Tracker Green and then washed three times with imaging saline and imaged at 37°C.

Antibody and Qdot labeling

HEK cells were labeled in imaging saline containing an anti-HA monoclonal antibody conjugated to Alexa Fluor 594 (1:1000 dilution) for 5–10 min at 37°C before being rinsed and imaged at 37°C. Quantum dot recycling assays were performed essentially as described previously (Deutsch *et al.*, 2012). Briefly, cells expressing biotinylated Kv1.3 or Kv1.4 constructs were first incubated in 1% bovine serum albumin (BSA; immunoglobulin G/fatty acid-free; Sigma-Aldrich, St. Louis, MO) in imaging saline for 5 min and then incubated for 5 min with 0.1 nM streptavidin-conjugated quantum dots (QD605; Invitrogen, Carlsbad, CA) in imaging saline containing 1% BSA. The cells were then rinsed extensively with imaging saline and returned to the tissue culture incubator. All incubations were performed at 37°C. To control for nonspecific Qdot binding, we imaged cells expressing GFP-Kv1.4-loopBAD that were not cotransfected with the BirA biotin ligase.

Detection of Kv1.4 recycling

The dissociation rate of biotin–streptavidin binding is relatively slow, with 4 and 25% dissociation over 1 h at 37°C for biotin conjugates or biotin, respectively (Howarth *et al.*, 2006; Chivers *et al.*, 2010). This slow dissociation rate, combined with the lack of photobleaching and low potential for biological degradation (Jaiswal *et al.*, 2004; Jaiswal and Simon, 2004), make Qdot labeling useful for tracking individual Kv channels to and from the cell surface. HEK cells expressing biotinylated Kv1.4 channels were labeled with Qdots at low efficiency, as described above, and then returned to the tissue culture incubator for 1–2 h to allow endocytosis and recycling to the cell surface to approach steady state. The cells were then removed from the incubator and imaged using the TIRF system described above. Spontaneous Qdot appearance represents a cytoplasmic channel previously on the cell surface now entering the 100-nm TIRF illumination field, that is, approaching or inserting into the membrane. Observation of the expected single-channel diffusion in the membrane confirmed surface delivery (Deutsch *et al.*, 2012). Spontaneous loss of a cell surface Qdot represents a channel undergoing endocytosis.

Image presentation and data analysis

Images were imported into Volocity 6.1.1 software for three-dimensional reconstruction, object detection/tracking, and quantitative analysis. Numerical data were exported into Origin Pro 8.5 (OriginLabs, Northampton, MA) for further analysis and curve fitting. Image sequences were analyzed for the location of Qdot appearance (i.e., membrane insertion) or disappearance (i.e. endocytosis) by both manual inspection and an automated analysis. In the case of the manual analysis, Qdots that appeared or disappeared within 2 µm of the cell perimeter were not counted, due to concerns that they might be just entering or leaving the basal cell surface. Qdots were classified as entering or leaving the surface at the cER if the appearance or disappearance occurred within 0.15 µm of the cER perimeter. Potential dark states <60 s were most problematic and were dealt with as described previously (Deutsch *et al.*, 2012). Only Qdot appearances that occurred more than 60 s following the disappearance of a Qdot within a 1 µm radius were counted as indicating surface insertion, as opposed to representing detection of the same Qdot emerging from a dark state. The same logic applied to Qdots that disappeared only to be followed by reappearance in <60 s <1 µm away; that is, these Qdots were not counted as being internalized by the cell.

For the automated detection and tracking of Qdot-labeled Kv1.4 channels, we used a multiple-target tracking (MTT) approach based on the algorithm developed by Sergé *et al.* (2008) and described previously (Deutsch *et al.*, 2012). This analysis provides the positions and intensities for each of the targets throughout the entire video duration, allowing for determination of the time and location of newly arriving channels to the cell surface. Using the results of the MTT algorithm, we categorized Qdot-tagged Kv1.4 channels that arrived to the cell surface after a delay relative to the start of the image sequence (to allow for potential Qdot dark states) as arriving to the cER or not. This classification was determined by overlaying the individual Qdot-tagged channel signal with the thresholded DsRed2-ER signal, along with the MTT algorithm trajectories. If the channel arrived within 1 pixel of the cER perimeter (1 pixel = 160 nm), it was categorized as arriving to the ER, and similarly if the channel appeared outside the 1 pixel boundary it was classified as not arriving to the cER. Channels that appeared to diffuse from the side of the cell to the basal surface were discarded.

TfR-SEP exocytosis

HEK cells or neurons were transfected with TfR-SEP and DsRed2-ER 18–24 h prior to imaging at 37°C. Basal SEP fluorescence was bleached for 1 min in TIR using 100% 488-nm laser power. SEP and DsRed fluorescence were imaged at a rate of 2 and 0.1 Hz, respectively, until SEP fluorescence recovered to a point at which additional exocytic events were masked. The center of each exocytic event, based on pixel intensity, was manually detected.

YFP-VSVG-ts045 exocytosis

HEK cells transfected with YFP-VSVG-ts045 and DsRed2-ER were cultured at the nonpermissive temperature of 40°C for 12–16 h prior to imaging and shift to the permissive temperature of 32°C. YFP and DsRed2 were imaged in TIR at a rate of 2 Hz and 0.1 Hz, respectively. Vesicles were tracked manually in Volocity.

Thin-section electron microscopy

HEK cells were grown on carbon-coated glass coverslips coated with Matrigel and fixed with 2.5% glutaraldehyde in 0.15 M phosphate buffer (pH 7.4). Coverslips were en bloc stained with aqueous uranyl acetate, postfixed with osmium tetroxide, and dehydrated with ethanol before being embedded in Epon. The carbon coat affixed to the embedded cells allowed for unambiguous orientation of the basal surface of the HEK cells for ultramicrotomy. Ultrathin sections (<100 nm) were mounted on copper grids and were imaged with a JEOL 1400 TEM.

Generation of EDMs

Locations of TfRs were determined using the U-track algorithm. For generation of the EDMs, images of the ER were processed using ImageJ (National Institutes of Health, http://imagesj.nih.gov/ij) in a two-step process that includes image segmentation followed by actual EDM transform. First, a value representing the level of extracellular background noise was subtracted from the image. Then, for correcting for heterogeneous background arising from cellular autofluorescence, the local background was found using a 20-pixel Gaussian filter, and it was subsequently subtracted from the original image. Next images were convolved with a 5×5 Laplacian kernel that acted as an edge detector to extract ER features. Images were zoomed by a factor of 10 using bicubic interpolation, which allowed for a higher accuracy in the final EDM. The images were then converted to binary by thresholding. The EDM was generated by inverting the image and using the Distance Mapping operation in MATLAB (MathWorks, Natick, MA). We used a custom-written algorithm to extract the pixel value of the EDM at the site of TfR exocytosis. Control values were determined by selecting all EDM values within a region of interest encompassing either the entire TIRF footprint (determined using low-level TfR fluorescence as a mask for the cell region) or only the region most highly enriched in ER. For the local ER network analysis, the ROI was hand-drawn around the ER. Distances from the ER were imported into Origin 8.6 for further analysis.

Statistics

Data are presented as the mean ± SD, unless otherwise indicated. Colocalization statistics were calculated in Volocity 6.1.1 only from intensity values within thresholds using the Pearson's correlation coefficient, as previously described (Barlow *et al.* 2010). Cumulative distribution functions of the distances to the cER were generated using a bin size of 75 nm. The distributions of the EDM and the distances from the delivery locations to the cER were compared using a two-sample *t* test.

ACKNOWLEDGMENTS

We thank Kim Davidson, Tom Yasamura, and John Rash for their assistance with thin-section EM. We also thank Jennifer Lippincott-Schwartz for kindly providing the GFP-CB5 plasmid. This work was supported by the National Institutes of Health under Grants RO1GM84136 and RO1GM084136S1 awarded to M.M.T. and RO1NS082271 awarded to M.J.K. and by the National Science Foundation under Grant PHY-0956714 awarded to D.K.

REFERENCES

Antonucci DE, Lim ST, Vassanelli S, Trimmer JS (2001). Dynamic localization and clustering of dendritic Kv2.1 voltage-dependent potassium channels in developing hippocampal neurons. Neuroscience 108, 69–81.

Barlow AL, Macleod A, Noppen S, Sanderson J, Guerin CJ (2010). Colocalization analysis in fluorescence micrographs: verification of a more accurate calculation of Pearson's correlation coefficient. Microsc Microanal 16, 710–724.

Bellve KD, Leonard D, Standley C, Lifshitz LM, Tuft RA, Hayakawa A, Corvera S, Fogarty KE (2006). Plasma membrane domains specialized for clathrin-mediated endocytosis in primary cells. J Biol Chem 281, 16139–16146.

Cao H, Krueger EW, McNiven MA (2011). Hepatocytes internalize trophic receptors at large endocytic "hot spots." Hepatology 54, 1819–1829.

Carrasco S, Meyer T (2011). STIM proteins and the endoplasmic reticulum-plasma membrane junctions. Annu Rev Biochem 80, 973–1000.

Chivers CE, Crozat E, Chu C, Moy VT, Sherratt DJ, Howarth M (2010). A streptavidin variant with slower biotin dissociation and increased mechanostability. Nat Methods 7, 391–393.

Deutsch E, Weigel AV, Akin EJ, Fox P, Hansen G, Haberkorn CJ, Loftus R, Krapf D, Tamkun MM (2012). Kv2.1 cell surface clusters are insertion platforms for ion channel delivery to the plasma membrane. Mol Biol Cell 23, 2917–2929.

Du J, Tao-Cheng JH, Zerfas P, McBain CJ (1998). The K^+ channel, Kv2.1, is apposed to astrocytic processes and is associated with inhibitory postsynaptic membranes in hippocampal and cortical principal neurons and inhibitory interneurons. Neuroscience 84, 37–48.

Ehrlich M, Boll W, Van Oijen A, Hariharan R, Chandran K, Nibert ML, Kirchhausen T (2004). Endocytosis by random initiation and stabilization of clathrin-coated pits. Cell 118, 591–605.

Gaidarov I, Santini F, Warren RA, Keen JH (1999). Spatial control of coated-pit dynamics in living cells. Nat Cell Bio 1, 1–7.

Hopkins CR (1985). The appearance and internalization of transferrin receptors at the margins of spreading human tumor cells. Cell 40, 199–208.

Howarth M, Chinnapen DJ-F, Gerrow K, Dorrestein PC, Grandy MR, Kelleher NL, El-Husseini A, Ting AY (2006). A monovalent streptavidin with a single femtomolar biotin binding site. Nat Methods 3, 267–273.

Jahn R, Sudhof TC (1999). Membrane fusion and exocytosis. Annu Rev Biochem 68, 863–911.

Jaiswal JK, Goldman ER, Mattoussi H, Simon SM (2004). Use of quantum dots for live cell imaging. Nat Methods 1, 73–78.

Jaiswal JK, Simon SM (2004). Potentials and pitfalls of fluorescent quantum dots for biological imaging. Trends Cell Biol 14, 497–504.

Jaqaman K, Loerke D, Mettlen M, Kuwata H, Grinstein S, Schmid SL, Danuser G (2008). Robust single-particle tracking in live-cell time-lapse sequences. Nat Methods 5, 695–702.

Jing SQ, Spencer T, Miller K, Hopkins C, Trowbridge IS (1990). Role of the human transferrin receptor cytoplasmic domain in endocytosis: localization of a specific signal sequence for internalization. J Cell Biol 110, 283–294.

Keller P, Toomre D, Diaz E, White J, Simons K (2001). Multicolour imaging of post-Golgi sorting and trafficking in live cells. Nat Cell Biol 3, 140–149.

Kennedy MJ, Davison IG, Robinson CG, Ehlers MD (2010). Syntaxin-4 defines a domain for activity-dependent exocytosis in dendritic spines. Cell 141, 524–535.

Klopfenstein DR, Kappeler F, Hauri HP (1998). A novel direct interaction of endoplasmic reticulum with microtubules. EMBO J 17, 6168–6177.

Liou J, Kim ML, Heo WD, Jones JT, Myers JW, Ferrell JE Jr., Meyer T (2005). STIM Is a Ca^{2+} sensor essential for Ca^{2+}-store-depletion-triggered Ca^{2+} influx. Curr Biol 15, 1235–1241.

Loerke D, Mettlen M, Yarar D, Jaqaman K, Jaqaman H, Danuser G, Schmid SL (2009). Cargo and dynamin regulate clathrin-coated pit maturation. PLoS Biol 7, e57.

Marchaland J, Cali C, Voglmaier SM, Li H, Regazzi R, Edwards RH, Bezzi P (2008). Fast subplasma membrane Ca^{2+} transients control exo-endocytosis of synaptic-like microvesicles in astrocytes. J Neurosci 28, 9122–9132.

McMahon HT, Boucrot E (2011). Molecular mechanism and physiological functions of clathrin-mediated endocytosis. Nat Rev Mol Cell Biol 12, 517–533.

McNiven MA (2006). Big gulps: specialized membrane domains for rapid receptor-mediated endocytosis. Trends Cell Biol 16, 487–492.

Mettlen M, Loerke D, Yarar D, Danuser G, Schmid SL (2010). Cargo- and adaptor-specific mechanisms regulate clathrin-mediated endocytosis. J Cell Biol 188, 919–933.

Miesenbock G, De Angelis DA, Rothman JE (1998). Visualizing secretion and synaptic transmission with pH-sensitive green fluorescent proteins. Nature 394, 192–195.

Miller K, Shipman M, Trowbridge IS, Hopkins CR (1991). Transferrin receptors promote the formation of clathrin lattices. Cell 65, 621–632.

Motley A, Bright NA, Seaman MN, Robinson MS (2003). Clathrin-mediated endocytosis in AP-2-depleted cells. J Cell Biol 162, 909–918.

Muennich EAL, Fyffe REW (2004). Focal aggregation of voltage-gated, Kv2.1 subunit-containing, potassium channels at synaptic sites in rat spinal motoneurones. J Physiol 554, 673–685.

Nunez D, Antonescu C, Mettlen M, Liu A, Schmid SL, Loerke D, Danuser G (2011). Hotspots organize clathrin-mediated endocytosis by efficient recruitment and retention of nucleating resources. Traffic 12, 1868–1878.

O'Connell KM, Loftus R, Tamkun MM (2010). Localization-dependent activity of the Kv2.1 delayed-rectifier K^+ channel. Proc Natl Acad Sci USA 107, 12351–12356.

O'Connell KM, Rolig AS, Whitesell JD, Tamkun MM (2006). Kv2.1 potassium channels are retained within dynamic cell surface microdomains that are defined by a perimeter fence. J Neurosci 26, 9609–9618.

O'Connell KM, Tamkun MM (2005). Targeting of voltage-gated potassium channel isoforms to distinct cell surface microdomains. J Cell Sci 118, 2155–2166.
Orci L, Gabbay KH, Malaisse WJ (1972). Pancreatic beta-cell web: its possible role in insulin secretion. Science 175, 1128–1130.
Orci L, Ravazzola M, Le Coadic M, Shen WW, Demaurex N, Cosson P (2009). From the cover: STIM1-induced precortical and cortical subdomains of the endoplasmic reticulum. Proc Natl Acad Sci USA 106, 19358–19362.
Petrini EM, Lu JY, Cognet L, Lounis B, Ehlers MD, Choquet D (2009). Endocytic trafficking and recycling maintain a pool of mobile surface AMPA receptors required for synaptic potentiation. Neuron 63, 92–105.
Presley JF, Cole NB, Schroer TA, Hirschberg K, Zaal KJ, Lippincott-Schwartz J (1997). ER-to-Golgi transport visualized in living cells. Nature 389, 81–85.
Rappoport JZ, Kemal S, Benmerah A, Simon SM (2006). Dynamics of clathrin and adaptor proteins during endocytosis. Am J Physiol Cell Physiol 291, C1072–C1081.
Robinson IM, Finnegan JM, Monck JR, Wightman RM, Fernandez JM (1995). Colocalization of calcium entry and exocytotic release sites in adrenal chromaffin cells. Proc Natl Acad Sci USA 92, 2474–2478.
Robinson IM, Yamada M, Carrion-Vazquez M, Lennon VA, Fernandez JM (1996). Specialized release zones in chromaffin cells examined with pulsed-laser imaging. Cell Calcium 20, 181–201.
Rosenbluth J (1962). Subsurface cisterns and their relationship to the neuronal plasma membrane. J Cell Biol 13, 405–421.
Russ JC (2007). The Image Processing Handbook, 5th ed., Boca Raton, FL: CRC.
Saffarian S, Cocucci E, Kirchhausen T (2009). Distinct dynamics of endocytic clathrin-coated pits and coated plaques. PLoS Biol 7, e1000191.
Schroeder TJ, Jankowski JA, Senyshyn J, Holz RW, Wightman RM (1994). Zones of exocytotic release on bovine adrenal medullary cells in culture. J Biol Chem 269, 17215–17220.
Sergé A, Bertaux N, Rigneault H, Marguet D (2008). Dynamic multiple-target tracing to probe spatiotemporal cartography of cell membranes. Nat Methods 5, 687–694.
Shaw G, Morse S, Ararat M, Graham FL (2002). Preferential transformation of human neuronal cells by human adenoviruses and the origin of HEK 293 cells. FASEB J 16, 869–871.
Spiliotis ET, Nelson WJ (2003). Spatial control of exocytosis. Curr Opin Cell Biol 15, 430–437.
Stenkula KG, Lizunov VA, Cushman SW, Zimmerberg J (2010). Insulin controls the spatial distribution of GLUT4 on the cell surface through regulation of its postfusion dispersal. Cell Metab 12, 250–259.
Sudhof TC (2004). The synaptic vesicle cycle. Annu Rev Neurosci 27, 509–547.
Sudhof TC, Rizo J (2011). Synaptic vesicle exocytosis. Cold Spring Harb Perspect Biol 3, a005637.
Stradalova V, Blazikova M, Grossmann G, Opekarova M, Tanner W, Malinsky J (2012). Distribution of cortical endoplasmic reticulum determines positioning of endocytic events in yeast plasma membrane. PLoS One 7, e35132.
Tamkun MM, O'Connell KM, Rolig AS (2007). A cytoskeletal-based perimeter fence selectively corrals a sub-population of cell surface Kv2.1 channels. J Cell Sci 120, 2413–2423.
Terasaki M, Chen LB, Fujiwara K (1986). Microtubules and the endoplasmic reticulum are highly interdependent structures. J Cell Biol 103, 1557–1568.
Toomre D, Steyer JA, Keller P, Almers W, Simons K (2000). Fusion of constitutive membrane traffic with the cell surface observed by evanescent wave microscopy. J Cell Biol 149, 33–40.
Waterman-Storer CM, Salmon ED (1998). Endoplasmic reticulum membrane tubules are distributed by microtubules in living cells using three distinct mechanisms. Curr Biol 8, 798–806.
Weigel AV, Simon B, Tamkun MM, Krapf D (2011). Ergodic and nonergodic processes coexist in the plasma membrane as observed by single-molecule tracking. Proc Natl Acad Sci USA 108, 6438–6443.
Wick PF, Trenkle JM, Holz RW (1997). Punctate appearance of dopamine-β-hydroxylase on the chromaffin cell surface reflects the fusion of individual chromaffin granules upon exocytosis. Neuroscience 80, 847–860.